Received: 24 November 2021 | Accepted: 23 June 2022

DOI: 10.1111/2041-210X.13942

Methods in Ecology and Evolution BRITISH ECOLOGICAL SOCIETY

RESEARCH ARTICLE

Spanning scales: The airborne spatial and temporal sampling design of the National Ecological Observatory Network

John Musinsky[1] | Tristan Goulden[1] | Gregory Wirth[2] | Nathan Leisso[2] | Keith Krause[1] | Mitch Haynes[1] | Cameron Chapman[1]

[1]National Ecological Observatory Network, Battelle, Boulder, CO, USA

[2]Ball Aerospace, Boulder, CO, USA

Correspondence
John Musinsky
Email: jmusinsky@battelleecology.org

Funding information
National Science Foundation, Grant/Award Number: 1724433

Handling Editor: Aaron Ellison

Abstract

1. Each year, the National Ecological Observatory Network's (NEON) Airborne Observation Platform (AOP) collects high-resolution hyperspectral imagery, discrete and waveform lidar, and digital photography at a subset of 81 terrestrial and aquatic research sites throughout the United States. These open remote sensing data, together with NEON in situ sensor measurements and field observations, enable researchers to characterize ecological processes at multiple spatial and temporal scales.
2. Here we describe the sampling design for the AOP that aims to meet the diverse research needs of the ecological science community within the operational constraints affecting airborne data collection. Our spatial sampling protocol captures NEON instrumented systems, field plots and environmental gradients around each site while considering the context of airspace restrictions and remote sensing instrument capabilities. We use time series of moderate resolution imaging spectroradiometer (MODIS) satellite and PhenoCam near-surface observations to define temporal sampling windows based on vegetation peak foliar greenness. We developed a probabilistic model based on MODIS reflectance imagery and Monte Carlo simulation to estimate sampling durations for cloud-free data collection at each site.
3. Agreement in the estimated phenophase transition dates between MODIS Enhanced Vegetation Index and PhenoCam Green Chromatic Coordinate varied by vegetation class. Results from both sensors show that some vegetation classes have relatively consistent interannual peak greenness start- and end-dates, while others experience high year-to-year variability in green-up and senescence. In addition to phenological variability among sites, certain vegetation forms demonstrate distinct, asynchronous responses to climate, resulting in non-overlapping peak greenness periods within a single site. Results from flight campaigns showed that the cloud-likelihood model underestimated actual cloud conditions by 13%–26%, depending on the probability used.
4. Where interannual or intra-site phenology is highly variable or clouds are a persistent problem, it becomes challenging to schedule domain deployments so that all sites are flown in cloud-free conditions while their vegetation communities are in peak greenness. Despite limitations, application of cloud and peak greenness

models to airborne sampling results in significant improvements to AOP data quality. Although most applicable to airborne sampling with hyperspectral and lidar instruments in piloted aircraft, these methods may be a valuable resource to deployment of Unmanned Aerial Vehicles for ecological research.

KEYWORDS
airborne remote sensing, cloud prediction, ecological sampling, phenology

1 | INTRODUCTION

The National Ecological Observatory Network (NEON) is a 30-year continental-scale ecological research facility sponsored by the National Science Foundation designed to collect and share scientific data that characterize and quantify how the nation's terrestrial and aquatic ecosystems are changing (Keller et al., 2008). The network includes 81 field sites (47 terrestrial and 34 aquatic) located in a range of representative ecosystems across the United States. The Observatory is composed of five measurement subsystems: the Terrestrial Instrument System (TIS), Terrestrial Observation System (TOS), Aquatic Instrument System (AIS), Aquatic Observation System (AOS) and Airborne Observation Platform (AOP) (Thorpe et al., 2016). At each field site, these subsystems collect a suite of highly calibrated and integrated in situ sensor measurements, field observations and airborne remote sensing data (Barnett, Adler, et al., 2019; Barnett, Duffy, et al., 2019; Elmendorf et al., 2016; Hinckley et al., 2016; Hoekman et al., 2017; Parker & Utz, 2022).

Operating three aircraft-mounted payloads similar to the Carnegie Airborne Observatory Airborne Taxonomic Mapping System (Asner et al., 2012), the NEON AOP acquires highly calibrated, co-registered sub-metre to metre-scale hyperspectral imagery, discrete and waveform lidar, and digital photography that complement NEON in situ observations for mapping vegetation states, structure and processes at regional scales around NEON field sites (Chadwick et al., 2020; Kampe, Asner, et al., 2010; Schaepman et al., 2009; Schimel et al., 2011). Covering landscapes that extend beyond the bounds of in situ field sampling, AOP remote sensing instruments acquire high spatial (<1 m) and spectral resolution (5 nm) data on upland watershed areas, diverse vegetation communities, natural and human disturbances and land management practices that may impact ecological processes within field sampling areas (Kampe, Johnson, et al., 2010). Remote sensing data collected by the AOP are used to generate 28 data products, many linked to TOS and AOS protocols and data products publicly available through the NEON data portal (data.neonscience.org) that support research from local to global scales (Nagy et al., 2021).

AOP remote sensing data have contributed to more than 78 peer-reviewed publications covering a wide range of ecological applications, including explorations into the relationships between vegetation structure and heterogeneity, plant foliar traits and processes such as carbon assimilation and habitat diversity (Chadwick et al., 2020; Kamoske et al., 2021; Marconi et al., 2021; Wang et al., 2020); improved forest inventories, tree-crown delineation and species identification (Ayrey & Hayes, 2018; Dalponte et al., 2019; Fricker et al., 2019; McMahon, 2019; Sumsion et al., 2019; Weinstein et al., 2021; Zou et al., 2019); refinements in canopy height modelling and biomass estimation (Khati et al., 2020; Liu et al., 2021); methods for measuring biodiversity (Carrasco et al., 2019; Kamoske et al., 2022; Scholl et al., 2021; Schweiger & Laliberté, 2022); geology and critical zone mapping (Brogan et al., 2019; Hermes et al., 2020; Wainwright et al., 2022); socio-environmental systems research (Ordway et al., 2021); and new remote sensing methods (Babadi et al., 2019; MacLean, 2017; Queally et al., 2021) among others (a complete list is available at neon.dimensions.ai/discover/publication).

This paper describes the spatial and temporal sampling design for the AOP that aims to provide standardized, high-quality remote sensing data capable of meeting the diverse range of research needs of the ecological science community, within the operational and environmental requirements and constraints affecting airborne data collection. We explore how airborne spatial sampling areas are delineated to capture landscape heterogeneity around NEON field sites and describe how temporal sampling windows are developed through historical analyses of vegetation phenology and cloud-cover to maximize the likelihood of acquiring high-quality data during the peak vegetation growth period ('peak greenness') at each site and in coordination with NEON field sampling teams. We detail how flight and instrument parameters configured to comply with federal aviation restrictions and safety standards may lead to trade-offs in data quality, and examine the accuracy of the models used to define temporal sampling windows and suggest ways these models could be improved. Finally, we review some of the approaches that might benefit users working with AOP data acquired under sub-optimal atmospheric conditions or marginal phenological windows.

Many of the processes described here build on the airborne planning methods in Kampe, Asner, et al. (2010) and Kampe, Johnson, et al. (2010) and were used to develop the planning approach in Chadwick et al. (2020); these methods have evolved in response to lessons learned during the Observatory construction and initial operations phases and through feedback from external scientists serving on NEON Technical Working Groups (TWGs). We recognize that a single sampling design cannot meet the needs of all research applications, but we hope this paper can serve as a community resource that enables a greater appreciation of the compromises and trade-offs inherent in airborne data collection and a better understanding of AOP data quality as it relates to data acquisition, while prompting recommendations

for sampling design improvements and algorithmic enhancements by researchers employing NEON data in their work.

2 | MATERIALS AND METHODS

2.1 | AOP instrumentation

Each of NEON AOP's remote sensing payloads currently consist of a NEON imaging spectrometer (NIS), an Optech Gemini, Optech Galaxy PRIME or Riegl Q780 small-footprint waveform-recording lidar, and a PhaseOne high-resolution digital camera. The NIS is a high fidelity visible-to-shortwave infrared spectrometer based on the next generation Airborne Visible Infrared Imaging Spectrometer (AVIRISng) designed to collect measurements of sunlight reflected from the Earth's surface in 426 spectral channels covering a range of wavelengths from 380 to 2,510 nm (Chapman et al., 2019). Since every chemically unique substance has a unique reflectance spectrum, the NIS can be used to identify plant species and traits, map vegetation health, detect disease or invasive species, and map drought and its impacts (Green et al., 1998; Ustin et al., 2004). The lidar is an active sensor that emits up to one million laser pulses per second at 1,064 nm and is used to map the ground surface, vegetation height and the vertical structure of leaves and branches within the canopy. The digital camera complements the other instruments by providing co-registered, high-resolution Red Green Blue (RGB) photographs of land cover, including roads, impervious surfaces and buildings. A precision global positioning system receiver and inertial measurement unit are incorporated for accurate recording of payload positioning and orientation during science data collection. Each payload is highly integrated, with the instruments mounted in a common, rigid frame installed in a DeHavilland DHC-6 Twin Otter, an aircraft selected for its relatively low survey speeds of 85–110 knots and ability to accommodate the AOP payload weight and volume (Figure 1).

NEON operates two payloads for the acquisition of science-quality data at NEON sites, and a third 'assignable asset' payload dedicated to surveys at locations specified by non-NEON researchers or to supplemental collections at NEON sites. The annual flight campaign season begins with instrument calibration in the AOP laboratory, followed by a series of calibration flights to collect baseline data for instrument alignment and performance verification (NEON, 2022a). After calibration flights, the payloads are deployed for science surveys across the NEON network. A typical flight campaign runs from March through October when each payload is deployed to a pre-determined set of domains, typically surveying all sites within each domain before moving to the next (information on AOP scheduling can be found at www.neonscience.org/data-collection/flight-schedules-coverage). Upon completion of science surveys, the payloads return to headquarters for a final set of calibration flights before de-installation from the aircraft. The instruments then undergo maintenance and laboratory calibration before returning to service in the next season's flight campaign.

2.2 | AOP flight parameters

The flight parameters for science surveys are largely determined by the need to produce metre-scale spectroscopy measurements for mapping individual overstory plants, achieve sufficient pulse density of discrete and waveform lidar returns for measuring vertical structure and the ground surface beneath dense canopies, balanced by the need for wide-area coverage around each site (requirements are not currently determined by camera specifications) (Table 1).

Nominal flight altitude is 1,000 m above-ground level (AGL). Minimum flight altitude is driven by the spectrometer contiguous sampling limits and lidar eye-safety requirements. At a planned aircraft speed of 50 m/s and a NIS sampling rate of 100 Hz, the along-track spacing between pixel centres on the ground is 0.5 m. With a fixed Instantaneous field of view (FOV) of 1 mrad, the minimum flight altitude producing a pixel of 0.5 m is 500 m AGL; flying lower would create data gaps in the along-track flight direction at nominal flight speed. A second requirement driving minimum flight altitudes is eye-safety. Each of the AOP lidars is a Class 3B or Class 4 laser producing infrared light, which presents a potential eye-safety hazard to ground observers. For eye-safety purposes, it is assumed

FIGURE 1 Top left—Twin Otter aircraft preparing for calibration flights; bottom left—Airborne Observation Platform payload installed in aircraft (instrument racks not shown); right—spectrometer, lidar and camera sensors viewed from below

TABLE 1 Sampling requirements related to data product generation

The Airborne Observation Platform (AOP) instrument ground sample distance must be planned to be 2 m or less
The AOP Imaging instrument sampling of the survey areas must be planned as contiguous or overlapping
AOP aerial data collection should be conducted at solar elevation angles of 40° or greater
AOP flight lines collected with <10% cloud-cover over the area of collect will be considered acceptable
AOP must plan aerial surveys of National Ecological Observatory Network terrestrial sites within 90% of the site's peak greenness

Source: Kampe, Asner, et al. (2010) and Kampe, Johnson, et al. (2010)

that a person on the ground may be viewing the aircraft during data collection using aided viewing equipment such as binoculars, and the aircraft must be above the extended nominal ocular hazard distance (eNOHD) to prevent injury (International Electrotechnical Commission, 2014). The eNOHD range depends on the laser pulse repetition rate (PRR) (number of pulses per second), the laser beam divergence (which drives the number of photons per m^2) and the laser power setting. In most laser configurations, the eNOHD of AOP lidars equals or exceeds the 500 m minimum AGL established by spectrometer sampling requirements, which further limits minimum flight altitude. Since low-to-medium laser power settings must be used to ensure eye-safety compliance, this can negatively affect canopy penetration and ground returns, and may require a reduced PRR, leading to lower pulse densities.

To provide wall-to-wall coverage over NEON flight boxes, flight lines are oriented in a north–south direction—regardless of terrain conditions—to reduce the contributions of view angle and sun-sensor geometries to bi-directional distribution function (BRDF) phenomena (nonlinear artefacts) in the imagery and provide consistency in flight line orientation between annual collections. North–south flight line orientation can result in large variations in flight line AGLs in the presence of variable terrain. The highest elevation along a flight line drives the altitude of the aircraft over mean sea level (MSL), which can produce larger than desired mean AGLs over the course of a line. We are currently experimenting with variable MSL flight lines that maintain relatively constant AGLs along the flight track at sites with highly variable terrain elevations. The lidar FOV is configured at a full scan angle of 37° to ensure complete lidar coverage beyond the spectrometer FOV of 34°. Usable overlap between adjacent lidar swaths is set at 37% to eliminate gaps between adjacent spectrometer swaths in the presence of terrain variation or significant turbulence.

2.3 | Determination of spatial sampling boundaries for the AOP

Up-scaling of both in situ and airborne measurements requires an airborne sampling design that (a) covers the 'area-of-influence' associated with the TIS cumulative eddy covariance flux tower instrumentation, TOS field observations and co-located AIS/AOS measurements; (b) captures landscape environmental representativeness and heterogeneity around field sites; and (c) is sensitive to temporal system variation (e.g. phenology). The criteria used in the protocol delineating airborne survey boundaries over each site result in datasets with adequate spatial extent to support the scaling of NEON field data to regional scales (Keller et al., 2008; Thorpe et al., 2016).

The airborne spatial sampling design process for terrestrial sites is as follows: A 10 km × 10 km minimum airborne sampling area ('flight box') is delineated over each terrestrial site, centred on the NEON tower and repositioned as necessary to capture the TOS sampling boundary and 90% cumulative eddy covariance flux and concentration footprints ('tower airshed') in their entirety. Since airflow will occasionally interact with vegetation of interest located outside of the tower airshed, a minimum 2 km distance is maintained between the tower and the edge of the flight box (Figure 2).

The horizontal placement of the 10 km × 10 km flight box may be visually adjusted to capture gradients in land cover, precipitation and temperature, elevation, and vegetation change adjacent to the TOS boundary that potentially influence field observations (Figure 3). For sites with TOS boundaries exceeding the minimum 10 km × 10 km sampling area, the flight box is expanded to cover the entire TOS boundary. This core sampling area becomes the Priority 1 flight box for data collection. (All flight boxes can be downloaded in ESRI shapefile or KMZ formats at www.neonscience.org/data-samples/data/spatial-data-maps.)

At certain sites, it may be necessary to expand airborne sampling to capture ecologically relevant areas outside the Priority 1 flight box (e.g. watershed extents for collocated aquatic sites or TOS boundaries). This expanded sampling area becomes the Priority 2 flight box. Assigning a lower flight collection priority to these areas improves flight operations efficiency in the event poor weather conditions prevent complete spatial coverage of a site during the annual flight campaign.

For terrestrial sites located in proximity to one another (DCFS & WOOD, KONZ & KONA, STEI & TREE) (see Table S1 for full site names), the 10 km × 10 km minimum area flight boxes are joined to create a single Priority 1 flight box that adheres to the airborne sampling criteria described above. For the 13 non-collocated aquatic sites (i.e. those not included within the survey areas of terrestrial sites), flight boxes are delineated to capture the entire watershed boundary upstream of aquatic instrumentation. Flight boxes for watersheds are truncated where surveys would exceed a single collection day in optimal weather conditions (ARIK, BLUE and SYCA), and may cover less than the 10 km × 10 km minimum size threshold for terrestrial sites. Finally, flight boxes for all sites may be modified in the future to accommodate ecosystem changes such as major disturbance events.

AOP flight parameters or spatial sampling boundaries at NEON sites may be impacted by Federal Aviation Administration (FAA) limits on flight activities over sensitive infrastructure and environmental

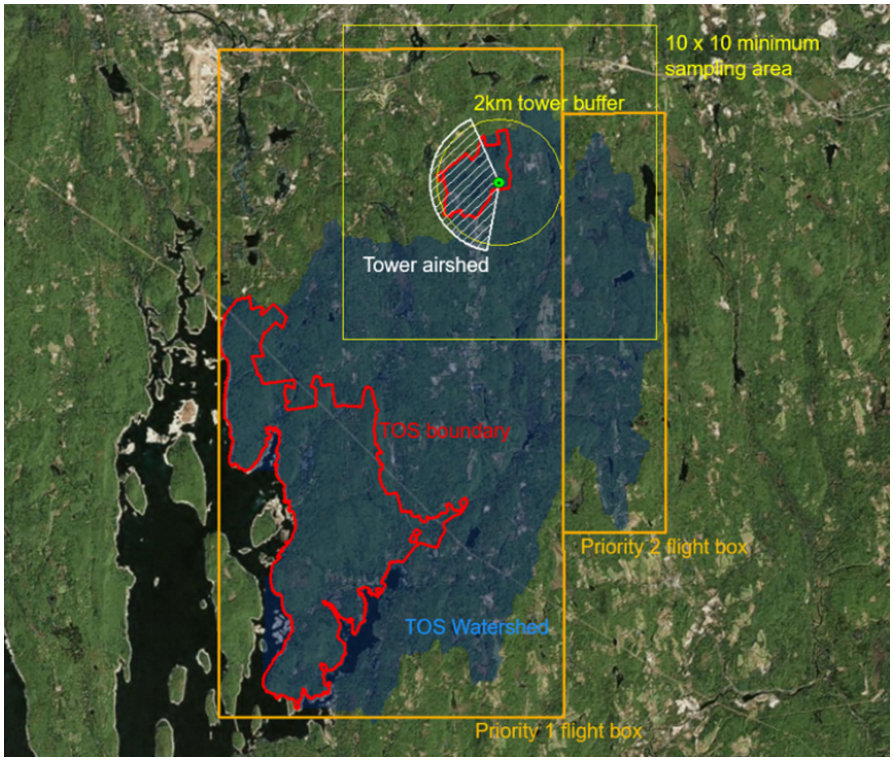

FIGURE 2 Priority 1 and 2 flight boxes for Harvard Forest

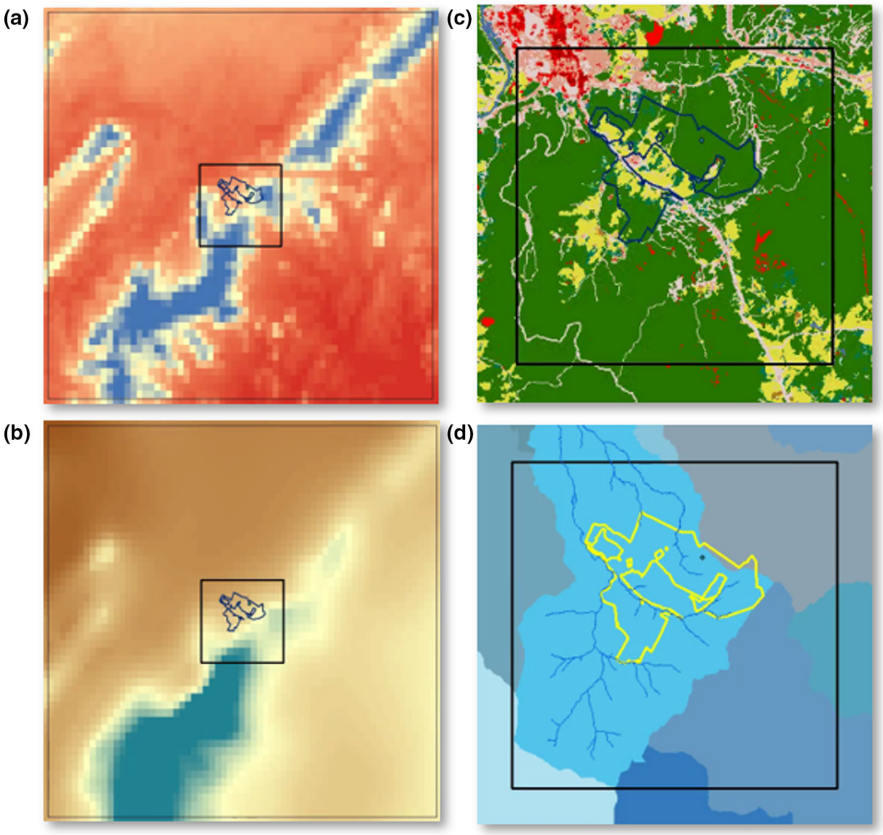

FIGURE 3 Environmental gradients used to optimize locations of Airborne Observation Platform flight boxes include (a) PRISM temperature and (b) PRISM precipitation (Di Luzio et al., 2008), (c) National Land Cover Database land cover (Homer et al., 2015) and forest change (Hansen et al., 2013), and (d) National Ecological Observatory Network-derived watershed boundaries

areas, both for safety and noise abatement reasons. Certain NEON sites are located within or adjacent to national parks (GRSM, RMNP, YELL) and wilderness areas (BART, MLBS, SCBI, SRER, TEAK) where the FAA requests that aircraft maintain a minimum altitude of 610 m (2,000 ft) AGL or greater (FAA Advisory Circular, 2004). This limits the minimum altitude AOP can fly over high-elevation areas, either

during data collection or while making turns between flight lines, which can result in flight lines exceeding the nominal mean 1,000 m AGL, reducing the spatial resolution of the Level 0 remote sensing data.

Additional airspace restrictions impacting AOP flight box design include Military Operations Areas (MOAs) and Restricted Areas established to separate hazardous and non-hazardous military activities from civilian air traffic. Sites effected by these restrictions include JORN, located adjacent to the White Sands Missile Range in New Mexico; DEJU, near the Buffalo Restricted Airspace and MOA in Alaska, and LAJA, within the airspace of a tethered aerostat radar system operated by U.S. Customs and Border Protection in Puerto Rico. Therefore, flight lines from JORN and DEJU do not cover the entire watershed extent, and from LAJA do not capture the entire TOS sampling area and deviate from a north–south orientation.

2.4 | Determination of temporal sampling windows for the AOP

The original NEON design called for annual surveys at all terrestrial sites. Reflecting budgetary limitations, surveys at NEON terrestrial sites are currently attempted a minimum of three of every 5 years during their peak greenness periods, except for those located in D20 (Hawaii) and D04 (Puerto Rico) which are surveyed at 5-year intervals due to high deployment costs. Each year canopy foliar chemistry sampling occurs at a rotating subset of 9–11 sites; these sites are always included in the annual flight campaign schedule. At all sites flown, certain field collection activities that link directly to AOP data products (e.g. canopy foliar chemistry sampling, aquatic water quality sampling) are scheduled to align with airborne surveys (Thorpe et al., 2016).

Three important constraints on the daily and seasonal temporal sampling windows of NEON airborne data collection are (a) the timing of acceptable solar elevation angles, (b) the cloud conditions present or anticipated during sampling and (c) the phenological state of dominant vegetation at each site. Scheduling of daily flights and seasonal campaign deployments requires accurate models of each of these factors; post-flight assessment of their state during data acquisition can help the end-user better understand data quality. (All data and processing code are available for download—see Musinsky et al., 2021.)

2.5 | Solar elevation angles

Most airborne mapping projects operating optical sensors are flown while solar angles exceed 30–45° to maximize surface-reflected solar radiance and minimize shadowing from topography and vegetation (Honkavaara et al., 2012; Pepe et al., 2018). AOP surveys most sites during daylight hours when solar angles exceed 40°; acceptable solar angles are relaxed to 35° at grassland and agricultural sites characterized by flat terrain and low vegetation, maintaining minimal shadowing in the imagery despite the lower solar elevation angle. At the northern latitude sites of Alaska, 35° solar angles are used by default due to limited 40° flight windows during summer months. Except for solar angle timings, no time-of-day constraints (e.g. avoiding solar noon during aquatic site surveys to minimize sun glint) are included in the sampling protocol.

2.6 | Cloud-cover

Changes to illumination conditions from clouds and aerosols greatly influence the quality of data produced by the spectrometer. To reduce the impact of atmospheric-induced degradation to the spectroscopy, AOP attempts to survey when cloud-cover represents less than 10% of sky coverage. Since many NEON sites are in regions where clouds are persistent during peak greenness periods, more days must be allocated to deployments to these sites to increase the likelihood of encountering cloud-free conditions.

Starting with the 2019 flight campaign, AOP implemented a probabilistic model to estimate the number of days required to collect cloud-free data given the number of flight hours needed to survey a site during acceptable solar angles. To better understand cloud patterns and trends at each site throughout the year, we calculated daily cloud-cover percentages for each Priority 1 flight box from a 16-year time series (2002–2017) of daily moderate resolution imaging spectroradiometer (MODIS) 1,000 m surface reflectance data (MOD09GA/MYD09GA Collection 6 from the Terra and Aqua satellites, whose overpass times are roughly concurrent with AOP morning and afternoon flights), using the *reflectance data state QA band*, where QA bits 0–1: Cloud State in the State_1km Bitmask are set to bit values of 1–3 (i.e. 'cloudy', 'mixed' and 'not set') (Roger et al., 2020). The total number of days per month per year where cloud-cover represented less than 10% of the Priority 1 flight box for each site during at the time of daily MODIS overpass was then calculated, and from this the mean percentage of cloud-free days (<10% cloud-cover) per month (Table 2). Domain 20 was not included in the analyses since the flights are performed by an outside contractor.

To better utilize these cloud-free fractions as part of flight campaign scheduling, we developed a Monte Carlo simulation to determine the probabilities that flight deployments of specific durations would result in cloud-free data acquisitions during the months of the year coinciding with each site's peak greenness period. The Monte Carlo simulation draws from the probability density for a binomial distribution as follows:

$$P(N) = \left(\frac{n}{N}\right) p^N (1-p)^{n-N}, \quad (1)$$

where n is the number of trials (10,000 in this case), p is the probability of success (0.5, 0.625, 0.8, 0.9) of acquiring cloud-free data and N is the minimum number of flight-days required to complete the survey of a site based on the flight box area. We calculated the probability shown in Equation 1 for an increasing number of flight-days until our desired probability of success was reached. The associated cloud-free flight-day values per probability-of-success level were stored in probability-of-success

TABLE 2 Percent of days per month with <10% cloud-cover within each Airborne Observation Platform Priority 1 flight box (16-year mean)

Domain	Site	Jan	Feb	Mar	Apr	May	Jun	Jul	Aug	Sep	Oct	Nov	Dec
01	HARV	0.21	0.17	0.22	0.29	0.22	0.21	0.27	0.29	0.35	0.22	0.26	0.16
01	BART	0.02	0.05	0.14	0.20	0.20	0.16	0.09	0.16	0.32	0.26	0.21	0.05
02	SCBI	0.18	0.21	0.25	0.30	0.22	0.18	0.17	0.18	0.26	0.31	0.32	0.21
02	SERC	0.25	0.28	0.30	0.36	0.28	0.24	0.25	0.28	0.32	0.35	0.38	0.25
02	BLAN	0.23	0.26	0.31	0.31	0.28	0.25	0.22	0.24	0.30	0.32	0.33	0.23
03	OSBS	0.38	0.39	0.36	0.28	0.22	0.07	0.05	0.06	0.10	0.26	0.40	0.35
03	DSNY	0.37	0.32	0.29	0.24	0.20	0.06	0.05	0.04	0.06	0.20	0.34	0.33
03	JERC	0.40	0.37	0.38	0.41	0.33	0.19	0.15	0.13	0.27	0.43	0.51	0.36
04	GUAN	0.17	0.15	0.07	0.05	0.04	0.05	0.06	0.05	0.11	0.14	0.16	0.17
04	LAJA	0.28	0.22	0.12	0.07	0.03	0.03	0.05	0.06	0.09	0.12	0.21	0.31
05	STEI/TREE	0.06	0.21	0.26	0.29	0.25	0.20	0.23	0.23	0.33	0.25	0.16	0.03
05	UNDE	0.02	0.04	0.11	0.19	0.21	0.22	0.18	0.20	0.30	0.19	0.11	0.01
05	STEI-CHEQ	0.05	0.12	0.25	0.30	0.25	0.23	0.24	0.26	0.34	0.26	0.20	0.04
06	KONZ/KONA	0.33	0.35	0.33	0.34	0.33	0.40	0.40	0.42	0.48	0.48	0.43	0.30
06	UKFS	0.36	0.35	0.31	0.32	0.32	0.36	0.38	0.39	0.46	0.45	0.39	0.33
07	ORNL	0.25	0.22	0.29	0.31	0.23	0.21	0.14	0.23	0.37	0.37	0.37	0.25
07	GRSM	0.19	0.18	0.17	0.24	0.14	0.07	0.04	0.05	0.14	0.31	0.35	0.22
07	MLBS	0.10	0.08	0.20	0.25	0.14	0.10	0.06	0.06	0.19	0.29	0.28	0.11
08	TALL	0.37	0.31	0.34	0.37	0.28	0.18	0.13	0.23	0.36	0.47	0.45	0.31
08	DELA	0.37	0.32	0.34	0.36	0.30	0.18	0.11	0.25	0.34	0.46	0.44	0.32
08	LENO	0.39	0.32	0.35	0.35	0.28	0.18	0.12	0.22	0.31	0.47	0.48	0.30
09	WOOD/ DCFS	0.25	0.20	0.17	0.29	0.30	0.28	0.39	0.39	0.43	0.33	0.22	0.14
09	NOGP	0.24	0.29	0.25	0.32	0.34	0.33	0.46	0.46	0.49	0.34	0.30	0.19
10	CPER	0.31	0.31	0.40	0.34	0.32	0.53	0.53	0.54	0.57	0.49	0.45	0.30
10	STER	0.27	0.31	0.35	0.38	0.42	0.58	0.63	0.60	0.61	0.52	0.40	0.27
10	RMNP	0.02	0.03	0.11	0.13	0.14	0.29	0.22	0.23	0.34	0.35	0.16	0.04
11	CLBJ	0.47	0.45	0.41	0.41	0.36	0.37	0.44	0.45	0.44	0.51	0.52	0.43
11	OAES	0.53	0.47	0.45	0.46	0.42	0.44	0.52	0.49	0.54	0.52	0.57	0.46
12	YELL	0.03	0.09	0.11	0.08	0.10	0.26	0.46	0.40	0.43	0.20	0.05	0.02
13	NIWO	0.00	0.00	0.00	0.00	0.06	0.07	0.06	0.12	0.18	0.06	0.00	0.00
13	MOAB	0.42	0.42	0.54	0.48	0.52	0.71	0.60	0.55	0.61	0.62	0.58	0.39
14	SRER	0.60	0.57	0.67	0.76	0.79	0.78	0.41	0.43	0.55	0.71	0.68	0.56
14	JORN	0.62	0.66	0.66	0.71	0.73	0.77	0.57	0.61	0.59	0.69	0.70	0.56
15	ONAQ	0.20	0.17	0.16	0.20	0.32	0.53	0.49	0.47	0.53	0.44	0.30	0.18
16	WREF	0.07	0.13	0.09	0.14	0.19	0.27	0.59	0.53	0.45	0.29	0.12	0.07
16	ABBY	0.11	0.16	0.09	0.13	0.17	0.23	0.48	0.43	0.39	0.26	0.14	0.09
17	SJER	0.36	0.42	0.50	0.55	0.71	0.86	0.91	0.90	0.87	0.77	0.56	0.37
17	SOAP	0.43	0.37	0.37	0.35	0.54	0.77	0.83	0.85	0.79	0.65	0.50	0.37
17	TEAK	0.22	0.19	0.15	0.16	0.28	0.58	0.67	0.70	0.64	0.60	0.42	0.17
18	TOOL	0.31	0.36	0.31	0.40	0.40	0.37	0.28	0.23	0.21	0.26	0.27	0.11
18	BARR	0.08	0.11	0.07	0.18	0.19	0.16	0.26	0.13	0.04	0.01	0.11	0.00
19	BONA	0.22	0.16	0.45	0.40	0.24	0.21	0.14	0.19	0.26	0.13	0.12	0.25
19	DEJU	0.10	0.21	0.43	0.25	0.25	0.23	0.20	0.20	0.22	0.18	0.12	0.10
19	HEAL	0.13	0.20	0.26	0.26	0.24	0.14	0.13	0.19	0.19	0.17	0.12	0.15

tables (Table 3; Tables S2–S4) for cross-reference with the cloud-free days per month table, enabling calculations of total flight-days required during deployment in a given month. For example, based on historical MODIS data, an average of 28% of days in the month of May have less than 10% cloud-cover at TALL and it takes 1 day to survey the site under cloud-free conditions; therefore, rounding the percentage of cloud-free days up to 30%, Table 3 indicates that a total of seven flight-days should be scheduled if planning to fly TALL in May to ensure a 90% probability of successfully acquiring cloud-free data over the entire Priority 1 flight box.

For sites where field-based canopy foliar chemistry sampling coincident with AOP surveys is planned, we set cloud-free collection probabilities to 80% or 90%, while sites without foliar sampling are set to 50% or 62.5% probability. When the required flight-days per site are added to estimates for the required transit days between domains, no-fly days due to pilot rotation, spectrometer cooling days and aircraft maintenance days, the application of this approach results in a series of flight deployment windows for all sites selected to be flown (note that the required collections days for each site in a domain are additive to determine the total length of a collection period in a domain). The flight deployment windows are assembled into an optimized flight campaign schedule that maximizes the likelihood of cloud-free data collection during the peak greenness windows of each NEON site (Table S5).

2.7 | Phenology

Due to budget constraints and limited payload capacity, AOP only samples each site included in the seasonal flight schedule a maximum of once per year during the height of the growing season. To ensure remote sensing observations control for changes in vegetation due to natural phenological variations across multiple years, the initial NEON design specified that AOP sampling was to be limited to the period when the overstory of dominant vegetation at a site is at >90% peak photosynthetic capacity (Kampe, Johnson, et al., 2010; Schimel, 2013).

To delineate the peak greenness periods of different vegetation types at each site, we used Google Earth Engine (GEE) to produce time series of Enhanced Vegetation Index (EVI) calculated from MODIS imagery for land cover classes as defined by the 2011 USGS National Land Cover Database (NLCD), a dataset derived from 30 m Landsat data (Homer et al., 2015; Huete et al., 2002). For each major land cover class exceeding 20% of the total area of each NEON terrestrial site, we extracted Area-of-Interest (AOI) masks from the NLCD basemap, cropped to each site's Priority 1 flight box and TOS boundary, and resampled to 125 m using a majority filter so that the resolution of the input NLCD vegetation classes more closely matched the resolution of MODIS EVI data while reducing processing errors in GEE. An 18-year EVI time series (2003–2020) for each land cover AOI was extracted from 16-day EVI composites of 250 m MOD13Q1 (Terra) and MYD13Q1 (Aqua) Collection 6 using only those pixels tagged with Detailed QA Bitmask bit-01 equal to 00 (i.e. 'VI produced with good quality') (Didan et al., 2015; Huete, 1999). The mean EVI value of the AOI for each 8-day increment was then calculated, resulting in a maximum of 46 observations per year at 8-day intervals. These were smoothed using a LOESS locally weighted regression algorithm with a smoothing span of 0.25,

TABLE 3 Probability-of-success table—number of days required (survey days plus weather contingency) to achieve 90% probability of cloud-free data collection when minimum number of days to survey a site equals (n) and percent of monthly cloud-free days equals (p). (see Tables S2–S4 for 80%, 62.5% and 50% probabilities)

p	*n* = 1	*n* = 2	*n* = 3	*n* = 4	*n* = 5	*n* = 6	*n* = 7	*n* = 8	*n* = 9
0.05	46	77	None	None	None	None	None	None	None
0.10	22	38	51	66	79	91	None	None	None
0.15	15	26	34	43	52	59	69	77	85
0.20	11	19	25	32	39	44	51	56	64
0.25	8	15	20	25	30	35	40	45	50
0.30	7	12	16	21	25	29	33	37	41
0.35	6	10	14	18	21	25	28	32	35
0.40	5	9	12	15	18	22	24	27	30
0.45	4	8	11	13	16	19	21	24	27
0.50	4	7	9	12	14	17	19	21	24
0.55	3	6	8	11	13	15	17	19	21
0.60	3	5	7	9	11	13	15	17	19
0.65	3	5	7	9	10	12	14	16	17
0.70	2	4	6	8	9	11	13	14	16
0.75	2	4	6	7	9	10	12	13	15
0.80	2	3	5	6	8	9	11	12	13
0.85	2	3	5	6	7	9	10	11	12
0.90	1	3	4	5	7	8	9	10	11
0.95	1	2	4	5	6	7	8	9	10
1.00	1	2	3	4	5	6	7	8	9

a non-parametric approach that reduces noise by estimating a local regression at each point in the time series (Klosterman et al., 2014). The resulting datasets were used to produce both annual and 18-year mean EVI phenology curves for dominant vegetation classes at each site; these analyses are updated on a yearly basis.

Before finalizing peak greenness windows for each site (described below), we verified the 90% end-of-spring (EOS) and start-of-fall (SOF) phenophase transition thresholds for each NLCD class by visually inspecting available top-of-tower PhenoCam images from 2016 to 2020 from the National Phenology Network (NPN)—which include those collected from PhenoCams mounted on NEON towers—corresponding to the annual 90% MODIS EVI EOS and SOF dates at each site (Figure S1) (construction of NEON towers was completed in phases so PhenoCam data are not available for five complete years at all sites). Based on the size and colour of spring foliar growth, the images confirmed that 90% was an appropriate threshold to use for start-of-peak greenness (EOS) for all vegetation classes. In contrast, inspection of PhenoCam images showed that the threshold that best represented end-of-peak greenness (SOF) varied among vegetation class: 90% for grasslands, shrublands, agriculture and tundra, and 80% for deciduous broadleaf forest, evergreen forest, mixed forest and woody wetlands.

We determined peak greenness windows for each vegetation class by identifying EOS and SOF dates corresponding to 90% of the amplitude from start-of-spring (SOS) to the maximum value of the mean phenology curve in the 18-year mean EVI phenology curve (Figure 4). For this analysis, we assumed SOS to be the day of year when the largest rate of change of the slope occurred during the beginning of the green-up phase, calculated as the maximum value of the second derivative of the pre-peak phenological curve. We obtained the 90% value representing EOS by multiplying the amplitude (maximum value minus SOS value) by 0.9 and used the FORECAST linear regression function in Excel to determine the specific day-of-year (DOY) this 90% value was reached along the rising (pre-peak)

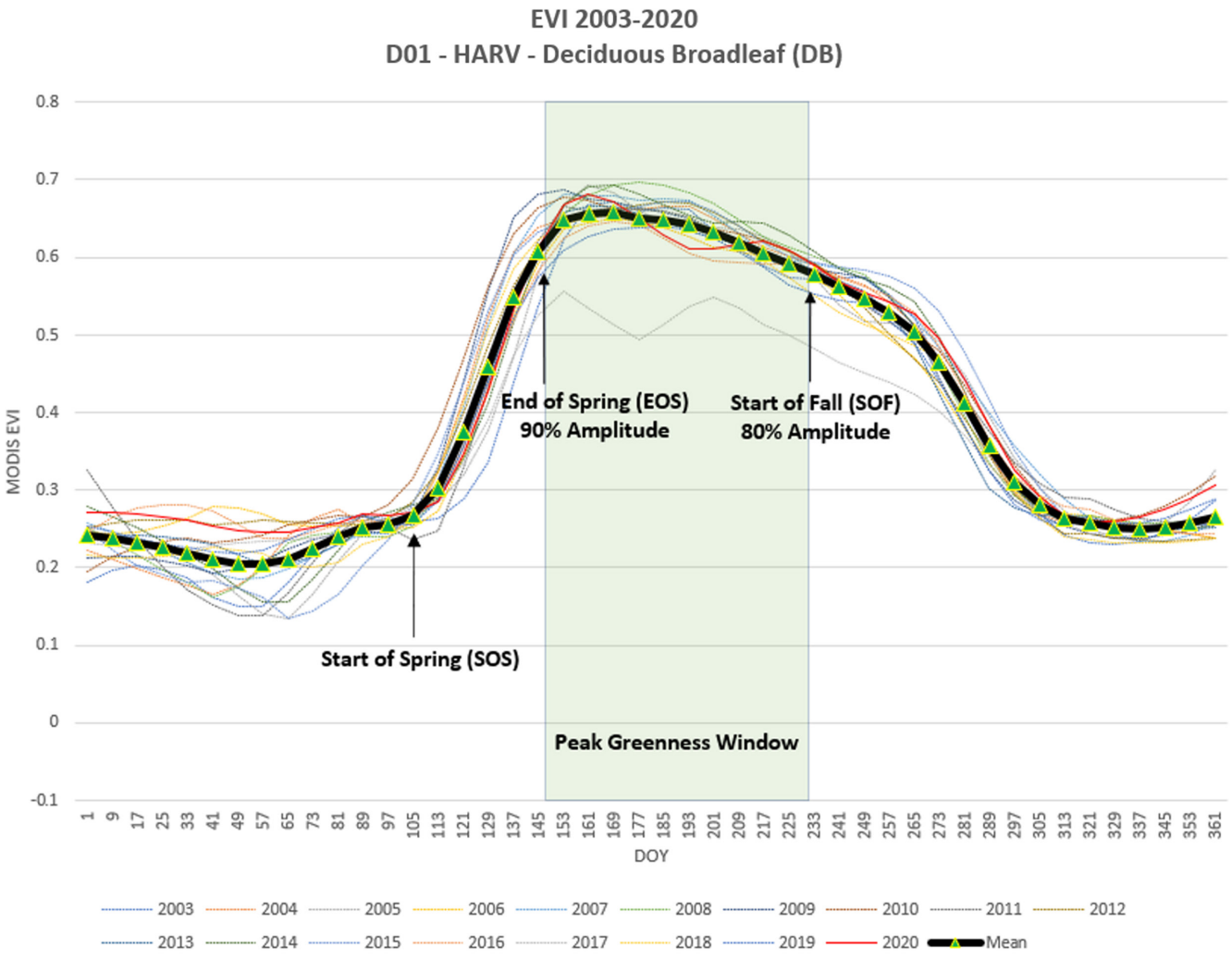

FIGURE 4 2003–2020 mean phenology and peak greenness window for deciduous broadleaf forest at Harvard Forest. Start-of-spring (SOS) calculated as the point of largest rate in change of slope (maximum value of the second derivative of the slope); end-of-spring calculated as 90% of the amplitude between SOS and the maximum mean Enhanced Vegetation Index (EVI) value; start-of-fall calculated as either 90% or 80% of the amplitude between SOS and the maximum mean EVI value, depending on vegetation type

slope of the mean phenology curve, interpolated between the DOYs associated with the sequential 8-day MOD13Q1 and MYD13Q1 DOY intervals.

Although most sites display a single phenological peak, certain sites are characterized by multiple phenological peaks. For these 'bi-modal' sites, we select the highest peak in the long-term mean for AOP data collection. At managed sites with more than one phenological peak (e.g. agricultural sites where multiple crop plantings occur), we estimated peak greenness windows for each phenological peak. Multiple deployments to these domains in a given year might be required if the none of the peak greenness periods of the agricultural sites aligned with the peak greenness periods of other sites in the same domain.

2.7.1 | Validation of MODIS EVI phenology

PhenoCam images can be used to create a Green Chromatic Coordinate (GCC) index that is analogous to EVI in its ability to measure seasonal phenological greenness patterns (Richardson, Hufkens, Milliman, & Frolking, 2018). To better understand the accuracy of MODIS EVI data as a planning tool, we compared the mean MODIS EVI EOS/SOF phenophase transition dates to the EOS/SOF transition dates extracted from PhenoCam GCC time series for matching NLCD cover classes. Since NLCD uses a different land cover classification scheme than the NPN, NLCD cover classes were first translated to NPN vegetation types (Table S1) (Richardson, Hufkens, Milliman, Aubrecht, et al., 2018). ***phenocamr*** PhenoCam processing software was used to download the top-of-tower 3-day summary product for each site from 2016 to 2020, iteratively smooth and interpolate the data and flag outliers, and extract the 90% EOS and 90%/80% SOF phenophase transition dates for each year based on the target NPN vegetation types (Hufkens et al., 2018; Seyednasrollah et al., 2019) (Figure 5).

3 | RESULTS

3.1 | Cloud-free data collection

To understand how well the cloud-free probabilities model performed in practice, we evaluated the success the AOP flight operations teams had in acquiring cloud-free data with deployments scheduled at the different probability thresholds. AOP defines a successful collection when 80% or more of the flight lines in a Priority 1 flight box are flown under <10% cloud-cover. Results from the 2019, 2020 and 2021 flight campaigns scheduled based on modelled probabilities of cloud-free data collection showed the model overestimated the likelihood—and underestimated the number of days required—of surveying NEON sites in cloud-free conditions by 13%–26% based on the actual number of flight lines AOP was able to collect (Figure 6).

3.2 | Peak greenness windows

3.2.1 | Spatial and temporal variability

Certain vegetation classes exhibit relatively consistent interannual peak greenness start- and end-dates, while others experience high year-to-year variability in green-up and senescence (Figure 7). The 90% EOS dates for deciduous broadleaf and evergreen needle forests were relatively consistent and predictable year-to-year in the EVI data, most likely because green-up and senescence are linked

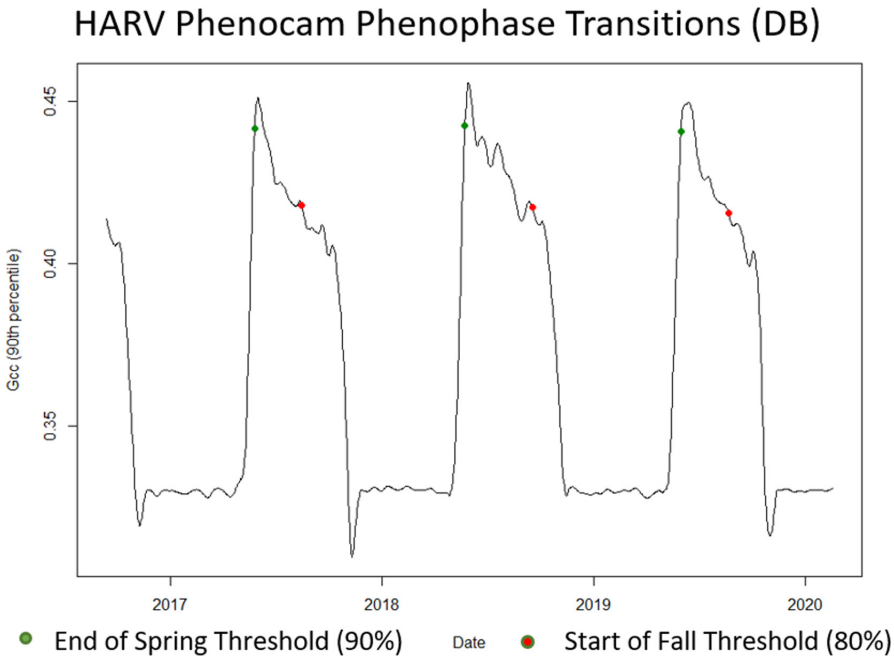

FIGURE 5 Example of 90% end-of-spring and 80% start-of-fall phenophase transition dates produced by phenocamr for deciduous broadleaf forest at Harvard Forest

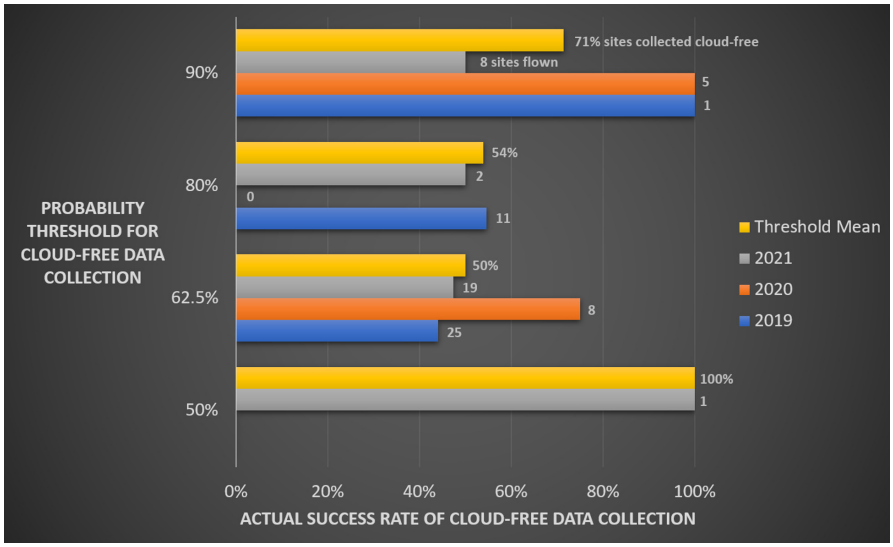

FIGURE 6 Successful collection of cloud-free data for deployments scheduled at different probability thresholds. Real-world results show that the modelled thresholds over-estimate the likelihood of acquiring cloud-free data and therefore under-estimate the number of days required to collect cloud-free data at a site.

to broad-scale seasonal changes in temperature and precipitation rather than short-term climate events. Grasslands were highly variable and less predictable, with green-up principally driven by rainfall and water abundance. Shrublands (including the desert southwest) displayed moderate variability, possibly due to the existence of precipitation-sensitive plants (e.g. grasses) growing among shrubs which cannot be distinguished at the observation scale of MODIS but are aggregated in the EVI data. Agricultural sites were variable due to management practices that closely track climate. Tundra sites in Alaska showed the greatest interannual consistency in phenophase transition dates.

In addition to phenological variability in dominant vegetation classes among sites, different vegetation classes at a single site may demonstrate distinct, asynchronous responses to seasonal temperature and precipitation patterns. While in most sites, the phenological peaks of dominant vegetation classes did overlap sufficiently to plan airborne surveys during the peak greenness periods of subdominant vegetation, at certain sites (e.g. DSNY—Figure 8) the peak growth periods for different vegetation classes were asynchronous in their timing, and the overlapping peak greenness windows short or non-existent.

3.2.2 | Accuracy of MODIS EVI phenology

Pairwise correlations between the >90% peak greenness start- (EOS) and end-dates (SOF) of mean MODIS EVI and mean PhenoCam GCC for 2016–2020 show that agreement was significantly greater for EOS than SOF and varied by vegetation class for both EOS and SOF (Figure 9). Although their sample sizes were small, shrub/scrub and tundra showed the closest agreement in both EOS and SOF. Grassland and deciduous broadleaf forest each displayed close agreement between EVI and GCC in EOS but not in SOF, while agreement was lowest in both EOS and SOF for evergreen needle forest.

3.2.3 | Surveys during actual vs. predicted peak greenness windows

During annual flight campaigns from 2016 to 2020, a total of 148 site surveys were collected, of which 116 surveys were scheduled within predicted peak greenness as determined by the 18-year mean EOS and SOF dates for the sites plus/minus the associated confidence intervals. The remaining 32 surveys were scheduled outside of peak greenness due to limited payload capacity (Table S6). Of the 116 surveys collected during predicted peak greenness, 85 surveys (73%) occurred during the actual peak greenness window for the respective year as determined retrospectively from MODIS EVI, while the actual peak greenness windows for 31 surveys (27%) varied from the predicted timeframes and the sites were collected outside of their actual peak greenness windows. Three additional surveys were collected outside of predicted peak greenness but inside actual peak greenness for that particular year. In terms of vegetation class, grassland was the most difficult to predict, accounting for 48% of the 'missed' peak greenness windows, followed by shrub/scrub (43%), tundra (27%), deciduous broadleaf forest (24%), evergreen needle forest (15%) and agriculture (0%) (both evergreen broadleaf forest surveys were flown outside of peak greenness).

4 | DISCUSSION

The AOP sampling design is a novel, data-driven approach towards managing the spatial and temporal complexity of the landscapes around NEON sites and the operational flight context in which sampling occurs. It represents a unique application of satellite and near-surface remote sensing and modelling in a framework that seeks to balance competing needs and constraints with the goal of optimizing multi-year data collection at a continental scale. We continually seek to improve our sampling strategy to provide high-quality remote sensing data efficiently and consistently over time, and results from the past 5 years of operational data collection at both NEON

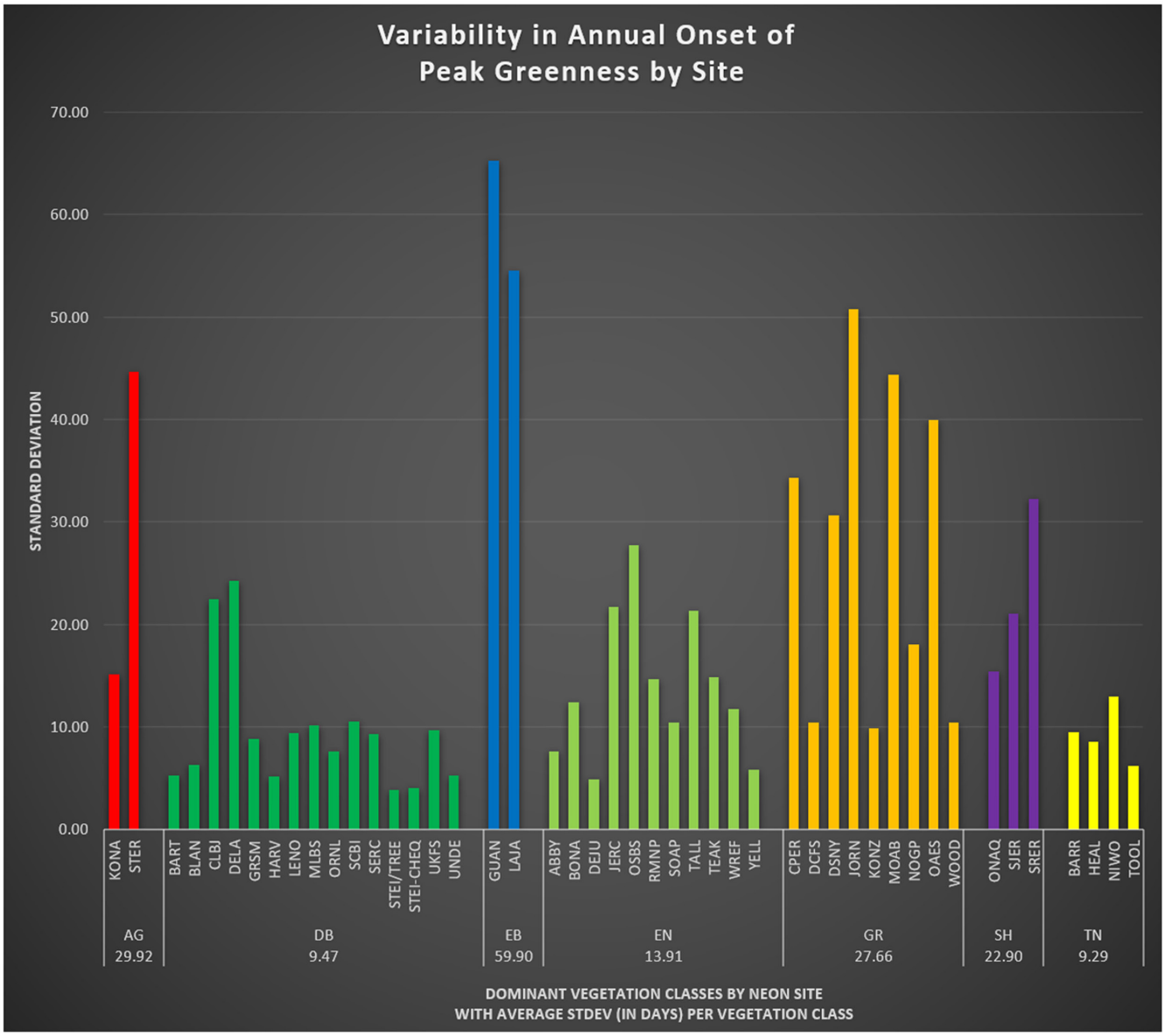

FIGURE 7 Measuring interannual variability: Standard deviations in onset (end-of-spring) of annual peak greenness windows from 18-year time series of moderate resolution imaging spectroradiometer (MODIS) Enhanced Vegetation Index. AG, agriculture; DB, deciduous broadleaf; EB, evergreen broadleaf; EN, evergreen needle; GR, grassland; SH, shrubland; TN, tundra. See Supporting Information for site name reference.

and non-NEON sites (e.g. Chadwick et al., 2020) give us a baseline on which to better understand the strengths and weaknesses in the current approach and develop refinements moving forward.

4.1 | Underestimation of cloud-free days

Although the sample size is limited, application of the cloud-free probabilities model showed it underestimated the actual number of days required to survey NEON sites in cloud-free conditions. One limitation is the lack of accurate thin-cirrus cloud detection. Cirrus can detrimentally affect spectral reflectance retrievals, and atmospheric correction algorithms generally perform poorly when cirrus clouds are present, so data collected under cirrus are considered >10% cloud-cover. However, the existence of thin cirrus layers can be difficult to identify in MODIS imagery, leading to optimistic estimates in the percentage of cloud-free days per month per site. A second error source is the model's reliance on MODIS imagery: cloud-cover changes constantly during the day, and since the MOD09GA/MYD09GA observations are essentially snapshots of cloud conditions at a moment in time they may not be representative of cloud conditions throughout a data collection flight. Wildfire smoke—an increasing problem throughout much of the country—is also not addressed by the cloud forecasting model. During the 2021 flight season, for example, wildfires in California and Washington State produced enough haze to convert most cloud-free data collection

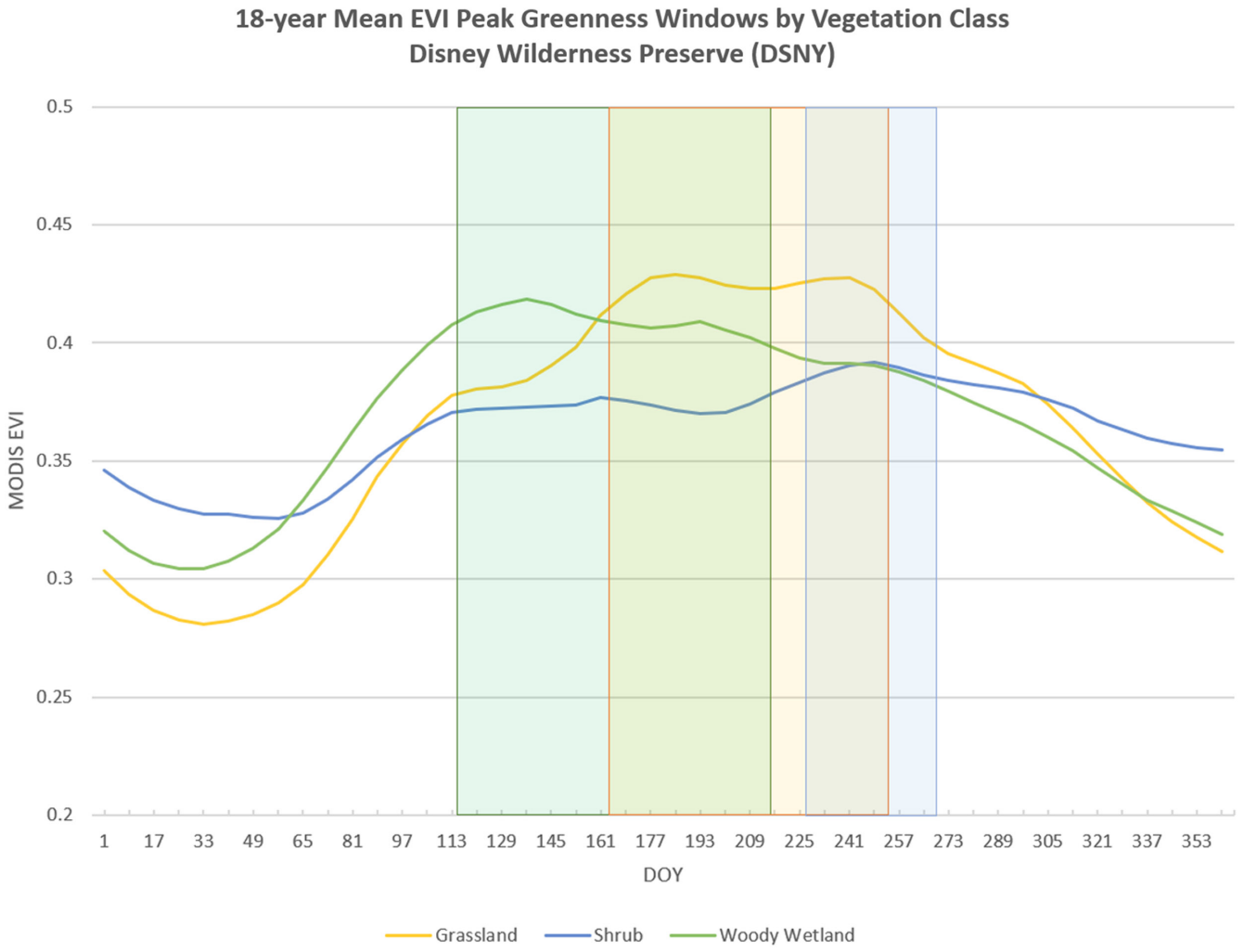

FIGURE 8 18-year mean Enhanced Vegetation Index phenology curves and their associated peak greenness windows for woody wetlands (green—day-of-year [DOY] 114–216), grasslands (yellow—DOY 163–255) and shrubs (blue—DOY 228–269) at Disney Wilderness Preserve

days into sub-optimal or no-fly days. Thus, limited high-quality spectrometer data were acquired at the Domain 16 and Domain 17 sites despite non-existent cloud-cover. Finally, simulations assume cloud-cover is an independent random process in both the temporal and spatial domains. However, weather patterns are likely to demonstrate temporal autocorrelation within the AOP collection window and spatial autocorrelation for sites within NEON domain boundaries, particularly if sites are in proximity or overlapping. To improve the accuracy of the cloud-probabilities model, we are refining cloud-cover estimates through finer-scale temporal mapping of cloud-cover using GOES 16/17 data to capture diurnal cloud dynamics, and modelling temporal and spatial autocorrelation to account for this behaviour.

4.2 | Uncertainty in Phenophase transition thresholds

There are several potential sources of error that contribute to uncertainty in our analysis of the timing of phenophase transitions. First, EVI measurements and their associated DOY within a 16-day MODIS composite can vary significantly, pixel-to-pixel, due to cloud-cover. Where clouds are persistent over the observation period of a 16-day composite image, cloud-free EVI observations from adjacent pixels may be acquired up to 16 days apart, which can bias the phenophase transition calculation—although this error may be reduced by using 8-day alternating MOD013Q1/MYD13Q1 data and averaging EVI across all pixels representing a particular vegetation class. Another source of potential error is spatial variability in green-up within a single vegetation class distributed across a flight box due to factors such as differences in elevation, soil moisture, etc. For example, studies have found approximately a one-day delay in EOS for every 30 m in elevation gain (e.g. White et al., 2014). We did not see such large variability in EVI when comparing pixels located in valleys to those on peaks in several mountainous sites, but this variability may have been reduced in the process of smoothing and averaging time-series data. There is also potential bias in our subjective interpretation of PhenoCam images to confirm the EOS/SOF transition thresholds

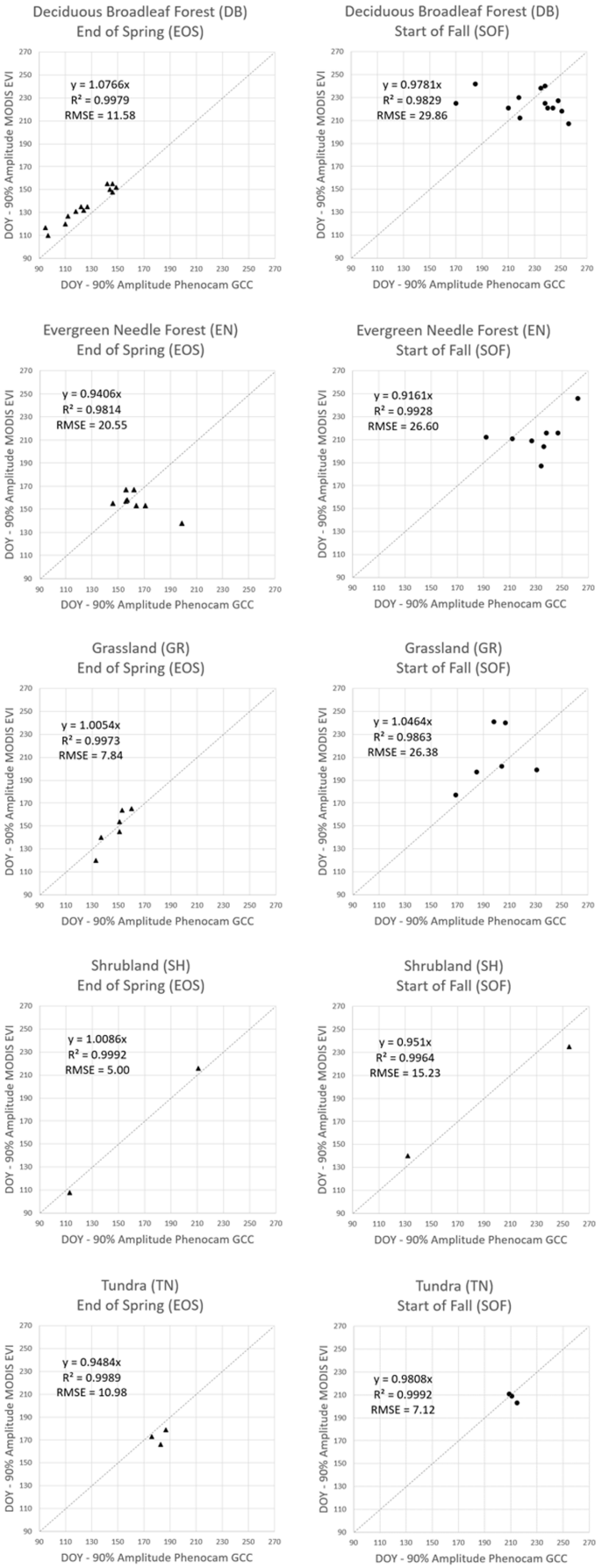

FIGURE 9 Pairwise correlations between end-of-spring and start-of-fall phenological transition dates from PhenoCam Green Chromatic Coordinate (GCC) and moderate resolution imaging spectroradiometer (MODIS) Enhanced Vegetation Index for deciduous broadleaf, evergreen needle, grassland, shrub and tundra vegetation classes. PhenoCam GCC indices are based on National Phenological Network image masks; MODIS enhanced vegetation indices are based on aggregated National Land Cover Database vegetation classes cropped by Priority 1 flight boxes.

that we applied categorically to the different vegetation classes. Finally, SOF typically exhibits greater uncertainty than EOS since changes to both colour and leaf area happen more gradually during fall transitions than spring.

While PhenoCam GCC results mostly corroborate the phenological patterns derived from MODIS, the use of near-surface observations as a validation source for satellite phenology observations is challenging. Disagreement in EOS/SOF between GCC and EVI may be due to different vegetation classes represented in PhenoCam ROIs than in the cropped NLCD land cover masks used to produce mean MODIS EVI values (Richardson, Hufkens, Milliman, & Frolking, 2018). NLCD classes are mapped from 30 m Landsat imagery, and separability among individual plants at this resolution is imprecise; this is exacerbated at the scale of 250 m MODIS data where a single EVI pixel can aggregate the phenological characteristics of spatially adjacent vegetation classes.

To improve the accuracy of peak greenness windows, we hope to explore other techniques for identifying phenophase transitions that may be more accurate than calculating a predetermined percent of the amplitude from SOS to maximum EVI or GCC. Zhang et al. (2018) employed the vegetation contrast index (VCI) which has greater dynamic range than GCC and is more sensitive to the amount of foliage present, while Donnelly et al. (2022) analysed site-specific phenometrics from NEON field observations with a new R package ***phenesse***, generating Weibull-parameterized estimates as part of their comparative study of in situ and remote sensing phenology. The sigmoid-based curve-fitting and pruned exact linear time change-point detection analysis employed by ***phenocamr*** might also prove superior; however, we tested these latter methods with MODIS EVI data in this study but ultimately did not adopt them due to repeated processing failures.

Uncertainty in EOS/SOF does impact the accuracy of deployment schedules. To minimize this impact, we have employed EOS/SOF confidence intervals (in days) for sites with long peak greenness periods, scheduling deployment start dates at least one-half the EOS confidence interval later than the mean peak greenness start-date and ending the deployment at least one-half the SOF confidence interval earlier than the peak greenness end-date. However, applying this to sites with short peak greenness periods can result in excessively narrow deployment windows, and certain sites (e.g. CPER) would have no dates to fly at all. While campaign schedules are prepared months in advance, AOP fortunately has some flexibility in the actual timing of surveys within domain deployment windows and uses real-time visual interpretation of PhenoCam images and GCC time series published by the NPN (phenocam.nau.edu) to make day-to-day decisions on whether a site is within peak greenness before executing a collection.

4.3 | Asynchronous plant phenology

Various studies have shown that different plant species at a site may exhibit different growth cycles (Donnelly et al., 2022; Pau et al., 2010). At sites where highly asynchronous phenology occurs among plant communities, AOP attempts surveys during the overlaps in peak greenness periods among vegetation classes. If that is not possible due to a lack of significant overlap, we survey during the mean peak greenness period of the dominant vegetation class found within the TOS boundary (e.g. deciduous broadleaf/woody wetlands in DSNY or tundra in NIWO).

A key assumption by NEON is that remote sensing data are comparable across years irrespective of the AOP collection dates if they are acquired above the EOS/SOF peak greenness thresholds. Depending on the science question, data for plant species in a state of early green-up or senescence and outside of their optimal sampling period may also be suitable for analysis. However, certain techniques, such as the retrieval of plant functional traits with hyperspectral data using radiative transfer model inversions or partial least squares, are affected by phenology across the peak growing season (Chlus et al., 2020; Schiefer et al., 2021), and data acquired outside of peak greenness may not meet the quality standards required for such analyses. Although data processing options may be limited for directly addressing this issue, because of operational constraints AOP frequently surveys sites in slightly different timeframes each year, and when combined with the natural interannual variability in vegetation phenology, plant communities that are phenologically marginal in a given year may be in peak greenness during another year's flight. For applications where data from shoulder seasons are problematic, researchers are encouraged to explore the historical time series of data at a site using PhenoCams, satellite vegetation indices or the R Shiny tool described below to verify that a target vegetation class of interest was in peak greenness during AOP flights.

4.4 | Sub-optimal data, sampling and data processing improvements

To ensure efficient data collection, after deploying to a domain AOP will typically wait for <10% cloud-cover before attempting surveys at a site. If weather forecasts indicate sub-optimal conditions through the end of the scheduled deployment, AOP will attempt a collection under >10% clouds to ensure complete flight box coverage with all instruments (lidar and camera data are unaffected by overhead clouds) and if sky conditions improve before scheduled transit to the next scheduled domain, AOP will make a second attempt to collect cloud-free data.

Only the highest quality data acquired during annual surveys at a site are published through the data portal, but this can include flight lines acquired under <10% and >10% cloud conditions, or a mix of both in the same dataset. Due to their impact to data quality, both weather conditions and phenological conditions during data acquisition are communicated in a variety of ways. During flights, airborne sensor operators record an estimate of total cloud-cover in three categories: (a) 0%–10% cloud-cover, (b) 10%–50% cloud-cover and (c) >50% cloud-cover, labelled as Green, Yellow and Red, respectively. The observed

weather classifications are stored in the HDF5 flight line files as attributes and converted into a weather quality image that represent different weather conditions among pixels in the mosaic tiles. Weather information is also communicated through a series of Google Earth KML files that depict each flight line coloured by the observed weather conditions. A table summarizing the flight lines acquired each day with the associated observed weather conditions is included in the L2 QAQC documents provided with data product downloads. Finally, we have developed *PhenoFlight*, an online R Shiny app that enables interactive exploration of the phenology and cloud-cover conditions during AOP data acquisition each year at each site (see Figure S2 for URL).

To improve cloud-free data collections while maximizing the number of sites flown each year, AOP is exploring application of a hybrid campaign model that combines fixed-schedule domain deployments to certain domains with 'hub-and-spoke' deployments to other domains where one domain serves as the base for deployments to its neighbours, taking advantage of short-term weather forecasts and the appearance of fair-weather windows in nearby domains to acquire cloud-free data outside of the scheduled deployment windows. We have also developed several GEE-based GOES cloud tracking tools (Figure S3) and a network of sky-facing cameras at NEON sites to assist with real-time monitoring of cloud conditions, further increasing the likelihood of cloud-free data collection.

As part of continuing efforts to improve data quality, we are planning to incorporate a BRDF correction algorithm into the processing pipeline producing L1 surface reflectance data, such as FlexBRDF (Queally et al., 2021). Although they are spatially limited relative to the AOP flight box footprint, we are exploring wider use of field spectral measurements (reflectance tarps and ASD spectroradiometer) and use of the Aeronet surface validation network—which includes the Cimel sun photometers mounted on NEON towers that measure direct solar irradiance and sky radiance—that provide inputs on aerosol transmission and scattering properties to the ATCOR atmospheric correction model employed by AOP (Wang et al., 2009). Further testing of processing techniques such as empirical line correction to improve hyperspectral surface reflectance products under varying cloud conditions may also be evaluated (Arroyo-Mora et al., 2021). More suitable for large-area surveys such as those performed by AOP is the potential integration of upward- and downward-looking solar spectral irradiance monitors on the aircraft similar to those developed and tested with AOP by the University of Colorado Boulder (Wright et al., 2021). These permit simultaneous irradiance measurements coincident with data collection during flight and allow for improved modelling and correction of the entire atmospheric column in both cloud-free and cloudy conditions. The ability to produce high-quality spectroscopy under cloud-cover would greatly increase the efficiency of flight operations, enabling more sites to be flown in a given year.

5 | CONCLUSIONS

Airborne remote sensing campaigns supporting a continental scale, site-based observatory such as NEON require detailed investigations into ecological conditions at local sites, consideration of the spatial and temporal extent of other sampling activities, an understanding of seasonal phenological patterns in vegetation and weather, and adherence to the resolution and accuracy requirements of data products. Optimizing each of these factors results in trade-offs that impact the flight parameters and sampling windows of NEON's AOP. Despite careful planning, unpredictable environmental disturbances (wildfires, droughts) and longer term changes due to an altering climate pose challenges to meeting all requirements. Since sampling optimizations are an ongoing process, we welcome feedback and contributions from the ecological and remote sensing science communities to improve this design, and encourage participation in the NEON TWGs that relate to the AOP (NEON, 2022b).

Although the survey footprints are typically much smaller, the spatial and temporal sampling approaches described here could be useful for planning Unmanned Aerial Vehicle (UAV) surveys aiming to study ecological dynamics in terrestrial environments. Projects utilizing UAVs with high-end payloads such as hyperspectral sensors are subject to the same constraints as AOP and may therefore benefit from the tools and code shared here that enable more precise pre-deployment planning, particularly when resources are limited. Additional criteria, such as surveys in periods of low wind and waves, or changes to payload instrument capabilities, might be necessary for improved airborne remote sensing of aquatic environments.

AUTHORS' CONTRIBUTIONS

J.M. developed the spatial and temporal sampling methodologies and software code, conducted the data analyses, and led flight campaign scheduling and flight planning; T.G. developed the statistical analyses and provided guidance in lidar sampling; G.W. developed the Monte Carlo modelling code for cloud-free probabilities; N.L. and K.K. developed spectrometer and lidar sampling requirements; M.H. and C.C. contributed to the implementation of flight campaign scheduling and flight planning; and J.M. and T.G. led the writing of the manuscript.

ACKNOWLEDGEMENTS

The National Ecological Observatory Network is a program sponsored by the National Science Foundation and operated under cooperative agreement by Battelle. This material is based in part upon work supported by the National Science Foundation through the NEON Program. We would like to thank past and current members of the AOP team for their efforts in making data collection and data products possible, as well as members of the Airborne Sampling Design Technical Working Group (TWG), the Airborne Remote Sensing Data Quality TWG, and the Lidar TWG for their feedback and guidance.

CONFLICT OF INTEREST

The authors certify that they have NO affiliations with or involvement in any organization or entity with any financial interest (such as

honoraria, patent or stock ownership, employment by a private company or membership of a company board of directors, consultancy or speaker's fees) or non-financial interest (such as personal or professional relationships) in the subject matter or materials discussed in this manuscript.

PEER REVIEW

The peer review history for this article is available at https://publons.com/publon/10.1111/2041-210X.13942.

DATA AVAILABILITY STATEMENT

Data and software code repositories associated with this manuscript are archived in GitHub and have been issued searchable DOI links through Zenodo at https://doi.org/10.5281/zenodo.5715477 and https://doi.org/10.5281/zenodo.5719760 (Musinsky et al., 2021). Detailed descriptions of data and software code, as well as URL links to custom tools mentioned in the manuscript, are documented in Supporting Information.

ORCID

John Musinsky https://orcid.org/0000-0002-1939-4666
Tristan Goulden https://orcid.org/0000-0001-9973-4079
Gregory Wirth https://orcid.org/0000-0001-9058-4860
Nathan Leisso https://orcid.org/0000-0003-0540-391X
Keith Krause https://orcid.org/0000-0002-2683-5239
Mitch Haynes https://orcid.org/0000-0001-8904-4840
Cameron Chapman https://orcid.org/0000-0003-0743-6336

REFERENCES

Arroyo-Mora, J. P., Kalacska, M., Løke, T., Schläpfer, D., Coops, N. C., Lucanus, O., & Leblanc, G. (2021). Assessing the impact of illumination on UAV pushbroom hyperspectral imagery collected under various cloud cover conditions. *Remote Sensing of Environment*, *258*(March), 112396. https://doi.org/10.1016/j.rse.2021.112396

Asner, G. P., Knapp, D. E., Boardman, J., Green, R. O., Kennedy-Bowdoin, T., Eastwood, M., Martin, R. E., Anderson, C., & Field, C. B. (2012). Carnegie Airborne Observatory-2: Increasing science data dimensionality via high-fidelity multi-sensor fusion. *Remote Sensing of Environment*, *124*, 454–465. https://doi.org/10.1016/j.rse.2012.06.012

Ayrey, E., & Hayes, D. J. (2018). The use of three-dimensional convolutional neural networks to interpret LiDAR for forest inventory. *Remote Sensing*, *10*(4), 1–16. https://doi.org/10.3390/rs10040649

Babadi, M., Sattari, M., & Iran Pour, S. (2019). Exploring the potential of full waveform airborne lidar features and its fusion with rgb image in classification of a sparsely forested area. *International Archives of the Photogrammetry, Remote Sensing and Spatial Information Sciences—ISPRS Archives*, *42*(4/W18), 147–152. https://doi.org/10.5194/isprs-archives-XLII-4-W18-147-2019

Barnett, D. T., Adler, P. B., Chemel, B. R., Duffy, P. A., Enquist, B. J., Grace, J. B., Harrison, S., Peet, R. K., Schimel, D. S., Stohlgren, T. J., & Vellend, M. (2019). The plant diversity sampling design for The National Ecological Observatory Network. *Ecosphere*, *10*(2). https://doi.org/10.1002/ecs2.2603

Barnett, D. T., Duffy, P. A., Schimel, D. S., Krauss, R. E., Irvine, K. M., Davis, F. W., Gross, J. E., Azuaje, E. I., Thorpe, A. S., Gudex-Cross, D., Patterson, M., McKay, J. M., McCorkel, J. T., & Meier, C. L. (2019). The terrestrial organism and biogeochemistry spatial sampling design for the National Ecological Observatory Network. *Ecosphere*, *10*(2). https://doi.org/10.1002/ecs2.2540

Brogan, D. J., MacDonald, L. H., Nelson, P. A., & Morgan, J. A. (2019). Geomorphic complexity and sensitivity in channels to fire and floods in mountain catchments. *Geomorphology*, *337*, 53–68. https://doi.org/10.1016/j.geomorph.2019.03.031

Carrasco, L., Giam, X., Papeş, M., & Sheldon, K. S. (2019). Metrics of lidar-derived 3D vegetation structure reveal contrasting effects of horizontal and vertical forest heterogeneity on bird species richness. *Remote Sensing*, *11*(7), 1–19. https://doi.org/10.3390/rs11070743

Chadwick, K. D., Brodrick, P. G., Grant, K., Goulden, T., Henderson, A., Falco, N., Wainwright, H., Williams, K. H., Bill, M., Breckheimer, I., Brodie, E. L., Steltzer, H., Williams, C. F. R., Blonder, B., Chen, J., Dafflon, B., Damerow, J., Hancher, M., Khurram, A., … Maher, K. (2020). Integrating airborne remote sensing and field campaigns for ecology and Earth system science. *Methods in Ecology and Evolution*, *11*(11), 1492–1508. 10.1111/2041-210X.13463

Chapman, J. W., Thompson, D. R., Helmlinger, M. C., Bue, B. D., Green, R. O., Eastwood, M. L., Geier, S., Olson-Duvall, W., & Lundeen, S. R. (2019). Spectral and radiometric calibration of the Next Generation Airborne Visible Infrared Spectrometer (AVIRIS-NG). *Remote Sensing*, *11*(18), 1–18. https://doi.org/10.3390/rs11182129

Chlus, A., Kruger, E. L., & Townsend, P. A. (2020). Mapping three-dimensional variation in leaf mass per area with imaging spectroscopy and lidar in a temperate broadleaf forest. *Remote Sensing of Environment*, *250*(February), 112043. https://doi.org/10.1016/j.rse.2020.112043

Dalponte, M., Frizzera, L., & Gianelle, D. (2019). Individual tree crown delineation and tree species classification with hyperspectral and LiDAR data. *PeerJ*, *2019*(1), e6227. https://doi.org/10.7717/peerj.6227

Di Luzio, M., Johnson, G. L., Daly, C., Eischeid, J. K., & Arnold, J. G. (2008). Constructing retrospective gridded daily precipitation and temperature datasets for the conterminous United States. *Journal of Applied Meteorology and Climatology*, *47*(2), 475–497. https://doi.org/10.1175/2007JAMC1356.1

Didan, K., Munoz, A. B., & Huete, A. (2015). MODIS Vegetation Index User's Guide (MOD13 Series).

Donnelly, A., Yu, R., Jones, K., Belitz, M., Li, B., Duffy, K., Zhang, X., Wang, J., Seyednasrollah, B., Gerst, K. L., Li, D., Kaddoura, Y., Zhu, K., Morisette, J., Ramey, C., & Smith, K. (2022). Exploring discrepancies between in situ phenology and remotely derived phenometrics at NEON sites. *Ecosphere*, *13*(1), 1–25. https://doi.org/10.1002/ecs2.3912

Elmendorf, S. C., Jones, K. D., Cook, B. I., Diez, J. M., Enquist, C. A. F., Hufft, R. A., Jones, M. O., Mazer, S. J., Miller-Rushing, A. J., Moore, D. J. P., Schwartz, M. D., & Weltzin, J. F. (2016). The plant phenology monitoring design for the National Ecological Observatory Network. *Ecosphere*, *7*(4), 1–16. https://doi.org/10.1002/ecs2.1303

FAA Advisory Circular No: 91-36D. (2004). Visual flight rules (VR) flight near noise-sensitive areas. Federal Aviation Administration, 17 September 2004.

Fricker, G. A., Ventura, J. D., Wolf, J. A., North, M. P., Davis, F. W., & Franklin, J. (2019). A convolutional neural network classifier identifies tree species in mixed-conifer forest from hyperspectral imagery. *Remote Sensing*, *11*(19), 1–22. https://doi.org/10.3390/rs11192326

Green, R. O., Eastwood, M. L., Sarture, C. M., Chrien, T. G., Aronsson, M., Chippendale, B. J., Faust, J. A., Pavri, B. E., Chovit, C. J., Solis, M., Olah, M. R., & Williams, O. (1998). Imaging spectroscopy and the Airborne Visible/Infrared Imaging Spectrometer (AVIRIS). *Remote Sensing of Environment*, *65*(3), 227–248. https://doi.org/10.1016/S0034-4257(98)00064-9

Hansen, M. C., Potapov, P. V., Moore, R., Hancher, M., Turubanova, S. A., Tyukavina, A., Thau, D., Stehman, S. V., Goetz, S. J., Loveland, T. R., Kommareddy, A., Egorov, A., Chini, L., Justice, C. O., & Townshend, J. R. G. (2013). High-resolution global maps of 21st-century forest cover change. *Science*, *342*, 850–853.

Hermes, A. L., Wainwright, H. M., Wigmore, O., Falco, N., Molotch, N. P., & Hinckley, E.-L. S. (2020). From patch to catchment: A statistical framework to identify and map soil moisture patterns across complex alpine terrain. *Frontiers in Water*, *2*(November), 1–17. https://doi.org/10.3389/frwa.2020.578602

Hinckley, E. L. S., Bonan, G. B., Bowen, G. J., Colman, B. P., Duffy, P. A., Goodale, C. L., Houlton, B. Z., Marí-Spiotta, E., Ogle, K., Ollinger, S. V., Paul, E. A., Vitousek, P. M., Weathers, K. C., & Williams, D. G. (2016). The soil and plant biogeochemistry sampling design for the National Ecological Observatory Network. *Ecosphere*, *7*(3), 1–15. https://doi.org/10.1002/ecs2.1234

Hoekman, D., Levan, K. E., Ball, G. E., Browne, R. A., Davidson, R. L., Erwin, T. L., Knisley, C. B., Labonte, J. R., Lundgren, J., Maddison, D. R., Moore, W., Niemela, J., Ober, K. A., Pearson, D. L., Spence, J. R., Will, K., & Work, T. (2017). Design for ground beetle abundance and diversity sampling within the National Ecological Observatory Network. *Ecosphere*, *8*(4). https://doi.org/10.1002/ecs2.1744

Homer, C., Dewitz, J., Yang, L., Jin, S., Danielson, P., Xian, G., Coulston, J., Herold, N., Wickham, J., & Megown, K. (2015). Completion of the 2011 national land cover database for the conterminous United States–Representing a decade of land cover change information. *Photogrammetric Engineering and Remote Sensing*, *81*(5), 345–354. https://doi.org/10.1016/S0099-1112(15)30100-2

Honkavaara, E., Markelin, L., Rosnell, T., & Nurminen, K. (2012). Influence of solar elevation in radiometric and geometric performance of multispectral photogrammetry. *ISPRS Journal of Photogrammetry and Remote Sensing*, *67*(1), 13–26. https://doi.org/10.1016/j.isprsjprs.2011.10.001

Huete, A., Didan, K., Miura, T., Rodriguez, E. P., Gao, X., & Ferreira, L. G. (2002). Overview of the radiometric and biophysical performance of the MODIS vegetation indices. *Remote Sensing of Environment*, *83*, 195–213. https://doi.org/10.1016/S0034-4257(02)00096-2

Huete, A. R. (1999). Modis vegetation index algorithm theoretical basis v3. Environmental Sciences, (mod 13).

Hufkens, K., Basler, D., Milliman, T., Melaas, E. K., & Richardson, A. D. (2018). An integrated phenology modelling framework in r. *Methods in Ecology and Evolution*, *9*(5), 1276–1285. https://doi.org/10.1111/2041-210X.12970

International Electrotechnical Commission. (2014). Safety of laser products—Part 1: Equipment classification and requirements. IEC 60825-1. Retrieved from https://webstore.iec.ch/publication/3587

Kamoske, A. G., Dahlin, K. M., Serbin, S. P., & Stark, S. C. (2021). Leaf traits and canopy structure together explain canopy functional diversity: An airborne remote sensing approach. *Ecological Applications*, *31*(2), e02230. Epub 2020 Nov 5. PMID: 33015908. https://doi.org/10.1002/eap.2230

Kamoske, A. G., Dahlin, K. M., Read, Q. D., Record, S., Stark, S. C., Serbin, S. P., & Zarnetske, P. L. (2022). Towards mapping biodiversity from above: Can fusing lidar and hyperspectral remote sensing predict taxonomic, functional, and phylogenetic tree diversity in temperate forests? *Global Ecology and Biogeography*, *March*, 1–21. https://doi.org/10.1111/geb.13516

Kampe, T. U., Asner, G. P., Green, R. O., Eastwood, M., Johnson, B. R., & Kuester, M. (2010). Advances in airborne remote sensing of ecosystem processes and properties: Toward high-quality measurement on a global scale. Proc. SPIE 7809, remote sensing and modeling of ecosystems for sustainability VII, 78090J (12 August 2010); https://doi.org/10.1117/12.859455

Kampe, T. U., Johnson, B. R., Kuester, M., & Keller, M. (2010). NEON: The first continental-scale ecological observatory with airborne remote sensing of vegetation canopy biochemistry and structure. *Journal of Applied Remote Sensing*, *4*(1), 043510. https://doi.org/10.1117/1.3361375

Keller, M., Schimel, D. S., Hargrove, W. W., & Hoffman, F. M. (2008). A continental strategy for the national ecological observatory network. *Frontiers in Ecology and the Environment*, *6*(5), 282–284. https://doi.org/10.1890/1540-9295(2008)6[282:ACSFTN]2.0.CO;2

Khati, U., Lavalle, M., Shiroma, G. H. X., Meyer, V., & Chapman, B. (2020). Assessment of forest biomass estimation from dry and wet SAR acquisitions collected during the 2019 UAVSAR AM-PM campaign in southeastern United States. *Remote Sensing*, *12*(20), 1–18. https://doi.org/10.3390/rs12203397

Klosterman, S. T., Hufkens, K., Gray, J. M., Melaas, E., Sonnentag, O., Lavine, I., Mitchell, L., Norman, R., Friedl, M. A., & Richardson, A. D. (2014). Evaluating remote sensing of deciduous forest phenology at multiple spatial scales using PhenoCam imagery. *Biogeosciences*, *11*(16), 4305–4320. https://doi.org/10.3390/rs13091722

Liu, A., Cheng, X., & Chen, Z. (2021). Performance evaluation of GEDI and ICESat-2 laser altimeter data for terrain and canopy height retrievals. *Remote Sensing of Environment*, *264*, 112571. https://doi.org/10.1016/j.rse.2021.112571

MacLean, M. G. (2017). Edge influence detection using aerial LiDAR in northeastern US deciduous forests. *Ecological Indicators*, *72*, 310–314. https://doi.org/10.1016/j.ecolind.2016.08.034

Marconi, S., Graves, S. J., Weinstein, B. G., Bohlman, S., & White, E. P. (2021). Estimating individual-level plant traits at scale. *Ecological Applications*, *31*(4), 1–15. https://doi.org/10.1002/eap.2300

McMahon, C. A. (2019). Remote sensing pipeline for tree segmentation and classification in a mixed softwood and hardwood system. *PeerJ*, *2019*(2), e5837. https://doi.org/10.7717/peerj.5837

Musinsky, J., Goulden, T., & Wirth, G. (2021). Supporting information, datasets, and R, python and JavaScript code for the National Ecological Observatory Network's airborne observation platform sampling design. https://doi.org/10.5281/zenodo.5715477, https://doi.org/10.5281/zenodo.5719760

Nagy, R. C., Balch, J. K., Bissell, E. K., Cattau, M. E., Glenn, N. F., Halpern, B. S., Ilangakoon, N., Johnson, B., Joseph, M. B., Marconi, S., O'Riordan, C., Sanovia, J., Swetnam, T. L., Travis, W. R., Wasser, L. A., Woolner, E., Zarnetske, P., Abdulrahim, M., Adler, J., … Zhu, K. (2021). Harnessing the NEON data revolution to advance open environmental science with a diverse and data-capable community. *Ecosphere*, *12*(12), 1–22. https://doi.org/10.1002/ecs2.3833

NEON (National Ecological Observatory Network). (2022a). Imaging Spectrometer. Retrieved from https://www.neonscience.org/data-collection/imaging-spectrometer

NEON (National Ecological Observatory Network). (2022b). Technical Working Groups. Retrieved from https://www.neonscience.org/about/advisory-groups/twgs

Ordway, E. M., Elmore, A. J., Kolstoe, S., Quinn, J. E., Swanwick, R., Cattau, M., Taillie, D., Guinn, S. M., Chadwick, K. D., Atkins, J. W., Blake, R. E., Chapman, M., Cobourn, K., Goulden, T., Helmus, M. R., Hondula, K., Hritz, C., Jensen, J., Julian, J. P., … Wilson, C. (2021). Leveraging the NEON Airborne Observation Platform for socio-environmental systems research. *Ecosphere*, *12*(6), 1–19. https://doi.org/10.1002/ecs2.3640

Parker, S. M., & Utz, R. M. (2022). Temporal design for aquatic organismal sampling across the National Ecological Observatory Network. *Methods in Ecology and Evolution*. https://doi.org/10.1111/2041-210X.13944

Pau, S., Okin, G. S., & Gillespie, T. W. (2010). Asynchronous response of tropical forest leaf phenology to seasonal and el niño-driven drought. *PLoS ONE*, *5*(6), e11325. https://doi.org/10.1371/journal.pone.0011325

Pepe, M., Fregonese, L., & Scaioni, M. (2018). Planning airborne photogrammetry and remote-sensing missions with modern platforms and sensors. *European Journal of Remote Sensing*, *51*(1), 412–435. https://doi.org/10.1080/22797254.2018.1444945

Queally, N., Ye, Z., Zheng, T., Chlus, A., Schneider, F., Ryan, P., & Townsend, P. A. (2021). FlexBRDF: A flexible BRDF correction for grouped processing of airborne imaging spectroscopy Flightlines. *Earth and Space Science Open Archive*, *May*, 1–27.

Richardson, A. D., Hufkens, K., Milliman, T., Aubrecht, D. M., Chen, M., Gray, J. M., Johnston, M. R., Keenan, T. F., Klosterman, S. T., Kosmala, M., Melaas, E. K., Friedl, M. A., & Frolking, S. (2018). Tracking vegetation phenology across diverse North American biomes using PhenoCam imagery. *Scientific Data*, *5*, 1–24. https://doi.org/10.1038/sdata.2018.28

Richardson, A. D., Hufkens, K., Milliman, T., & Frolking, S. (2018). Intercomparison of phenological transition dates derived from the PhenoCam dataset V1.0 and MODIS satellite remote sensing. *Scientific Reports*, *8*(1), 1–12. https://doi.org/10.1038/s41598-018-23804-6

Roger, J. C., Ray, J. P., & Vermote, E. F. (2020). MODIS collection 6.1 (C61) LSR product user. *Guident*, *1*, 1–36.

Schaepman, M. E., Ustin, S. L., Plaza, A. J., Painter, T. H., Verrelst, J., & Liang, S. (2009). Earth system science related imaging spectroscopy-an assessment. *Remote Sensing of Environment*, *113*(Suppl. 1), S123–S137. https://doi.org/10.1016/j.rse.2009.03.001

Schiefer, F., Schmidtlein, S., & Kattenborn, T. (2021). The retrieval of plant functional traits from canopy spectra through RTM-inversions and statistical models are both critically affected by plant phenology. *Ecological Indicators*, *121*(June 2020), 107062. https://doi.org/10.1016/j.ecolind.2020.107062

Schimel, D. (2013). NEON observatory design, NEON DOC 000001. Revision D. Retrieved from https://data.neonscience.org/documents/10179/11206/NEON.DOC.000001vD

Schimel, D.S., Keller, M., Berukoff, S., Kao, B., Loescher, H., Powell, H., Kampe, T., Moore, D., & Gram, W. (2011). *NEON science strategy: Enabling continental scale ecological forecasting*. NEON, Inc. Retrieved from https://www.researchgate.net/publication/236109188_NEON_Science_Strategy_Enabling_Continental-Scale_Ecological_Forecasting

Scholl, V. M., McGlinchy, J., Price-Broncucia, T., Balch, J. K., & Joseph, M. B. (2021). Fusion neural networks for plant classification: Learning to combine RGB, hyperspectral, and lidar data. *PeerJ*, *9*, 1–22. https://doi.org/10.7717/peerj.11790

Schweiger, A. K., & Laliberté, E. (2022). Plant beta-diversity across biomes captured by imaging spectroscopy. *Nature Communications*, *13*, 2767. https://doi.org/10.1038/s41467-022-30369-6

Seyednasrollah, B., Young, A. M., Hufkens, K., Milliman, T., Friedl, M. A., Frolking, S., & Richardson, A. D. (2019). Tracking vegetation phenology across diverse biomes using version 2.0 of the PhenoCam dataset. *Scientific Data*, *6*(1), 1–11. https://doi.org/10.1038/s41597-019-0229-9

Sumsion, G. R., Bradshaw, M. S., Hill, K. T., Pinto, L. D. G., & Piccolo, S. R. (2019). Remote sensing tree classification with a multilayer perceptron. *PeerJ*, *2019*(2), e6101. https://doi.org/10.7717/peerj.6101

Thorpe, A. S., Barnett, D. T., Elmendorf, S. C., Hinckley, E. L. S., Hoekman, D., Jones, K. D., Levan, K. E., Meier, C. L., Stanish, L. F., & Thibault, K. M. (2016). Introduction to the sampling designs of the National Ecological Observatory Network Terrestrial Observation System. *Ecosphere*, *7*(12), 1–11. https://doi.org/10.1002/ecs2.1627

Ustin, S. L., Roberts, D. A., Gamon, J. A., Asner, G. P., & Green, R. O. (2004). Using imaging spectroscopy to study ecosystem processes and properties. *Bioscience*, *54*(6), 523–534. https://doi.org/10.1641/0006-3568(2004)054[0523:UISTSE]2.0.CO;2

Wainwright, H. M., Uhlemann, S., Franklin, M., Falco, N., Bouskill, N. J., Newcomer, M. E., Dafflon, B., Siirila-Woodburn, E. R., Minsley, B. J., Williams, K. H., & Hubbard, S. S. (2022). Watershed zonation through hillslope clustering for tractably quantifying above-and below-ground watershed heterogeneity and functions. *Hydrology and Earth System Sciences*, *26*(2), 429–444. https://doi.org/10.5194/hess-26-429-2022

Wang, Y., Lyapustin, A. I., Privette, J. L., Morisette, J. T., & Holben, B. (2009). Atmospheric correction at AERONET locations: A new science and validation data set. *IEEE Transactions on Geoscience and Remote Sensing*, *47*(8), 2450–2466. https://doi.org/10.1109/TGRS.2009.2016334

Wang, Z., Chlus, A., Geygan, R., Ye, Z., Zheng, T., Singh, A., Couture, J. J., Cavender-Bares, J., Kruger, E. L., & Townsend, P. A. (2020). Foliar functional traits from imaging spectroscopy across biomes in eastern North America. *New Phytologist*, *228*, 494–511. https://doi.org/10.1111/nph.16711

Weinstein, B. G., Graves, S. J., Marconi, S., Singh, A., Zare, A., Stewart, D., Bohlman, S. A., & White, E. P. (2021). A benchmark dataset for canopy crown detection and delineation in co-registered airborne RGB, LiDAR and hyperspectral imagery from the National Ecological Observation Network. *PLoS Computational Biology*, *17*(7), 1–18. https://doi.org/10.1371/journal.pcbi.1009180

White, K., Pontius, J., & Schaberg, P. (2014). Remote sensing of spring phenology in northeastern forests: A comparison of methods, field metrics and sources of uncertainty. *Remote Sensing of Environment*, *148*, 97–107. https://doi.org/10.1016/j.rse.2014.03.017

Wright, L. A., Kindel, B. C., Pilewskie, P., Leisso, N. P., Kampe, T. U., & Schmidt, K. S. (2021). Below-cloud atmospheric correction of airborne hyperspectral imagery using simultaneous solar spectral irradiance observations. *IEEE Transactions on Geoscience and Remote Sensing*, *59*(2), 1392–1409. https://doi.org/10.1109/TGRS.2020.3003209

Zhang, X., Jayavelu, S., Liu, L., Friedl, M. A., Henebry, G. M., Liu, Y., Schaaf, C. B., Richardson, A. D., & Gray, J. (2018). Evaluation of land surface phenology from VIIRS data using time series of PhenoCam imagery. *Agricultural and Forest Meteorology*, *256–257*(March), 137–149. https://doi.org/10.1016/j.agrformet.2018.03.003

Zou, S., Gader, P., & Zare, A. (2019). Hyperspectral tree crown classification using themultiple instance adaptive cosine estimator. *PeerJ*, *2019*(2), 1–23. https://doi.org/10.7717/peerj.6405

SUPPORTING INFORMATION

Additional supporting information can be found online in the Supporting Information section at the end of this article.

How to cite this article: Musinsky, J., Goulden, T., Wirth, G., Leisso, N., Krause, K., Haynes, M., & Chapman, C. (2022). Spanning scales: The airborne spatial and temporal sampling design of the National Ecological Observatory Network. *Methods in Ecology and Evolution*, *13*, 1866–1884. https://doi.org/10.1111/2041-210X.13942